Lattice Boltzmann simulations of anisotropic permeabilities in carbon paper gas diffusion layers

Liang Hao [a,b], Ping Cheng [a,b,*]

[a] Ministry of Education Key Laboratory of Power Machinery and Engineering, Shanghai Jiaotong University, Shanghai 200240, PR China
[b] School of Mechanical and Power Engineering, Shanghai Jiaotong University, Shanghai 200240, PR China

ABSTRACT

The multiple-relaxation-time (MRT) lattice Boltzmann method (LBM) with multi-reflection solid boundary conditions is used to study anisotropic permeabilities of a carbon paper gas diffusion layer (GDL) in a fuel cell. The carbon paper is reconstructed using the stochastic method, in which various porosities and microstructures are achieved to simulate different samples. The simulated permeability and tortuosity show anisotropic characteristics of the reconstructed carbon papers with in-plane permeability higher than through-plane, and in-plane tortuosity lower than through-plane. The calculated permeabilities are in good agreement with existing measurements. The relationship between the permeability and the porosity is fitted with empirical relations and some fitting constants are determined. Furthermore, the obtained relationship of tortuosity and porosity is used in a fractal model for permeabilities. The results indicate that the fractal model and the Kozeny–Carman equation provide similar predictions on the through-plane permeability of the carbon paper GDL.

© 2008 Published by Elsevier B.V.

1. Introduction

Due to their high efficiency, low pollution and low noise, proton exchange membrane fuel cells (PEMFCs) have attracted much attention for over a decade as a promising candidate for power sources in automotive and other portable electronic devices. A typical PEMFC consists of a polymer membrane sandwiched between two electrodes (anode and cathode). Each electrode can be divided into three regions: the bipolar plate, the gas diffusion layer (GDL) and the catalyst layer. In PEMFCs, fuel and oxidant are supplied to the channels on the bipolar plate, and transfer through the gas diffusion layer to catalyst activity sites where electrochemical reactions occur. The GDL plays an important role for providing structural support, permeating reactant gas, removing product water and conducting electrons. The permeation of gas and removal of liquid water from GDL are critical to the performance of the PEMFCs, because higher reactant mass transfer rates would achieve higher current densities while the accumulation of liquid water in GDL would block reactant transfer, thus lowering the performance [1]. Therefore, the permeability of the GDL is a key parameter on the performance of the PEMFCs.

Generally, the GDL is a porous medium made of carbon paper or carbon cloth. These materials have microscopically complex structure with random distribution of pore sizes, ranging from a few microns to tens of microns. In practice, in order to decrease the resistance for the electrons transfer from the catalyst layer to the bipolar plane, the GDL is slightly compressed by external force, by which the permeability is reduced [2]. Experimental studies confirm that there exists an optimal compression for the GDL, attributing to the trade-off between the improved contact resistance and the reduced GDL permeability [3]. Additionally, it is believed that treating the GDL with a hydrophobic polymer such as PTFE would improve water removal and thus facilitate gas diffusion in the GDL. However, studies also show that electrical conductivity and permeability of the GDL are reduced if excessive PTFE is added [4], due to the insulating property of PTFE and the filling of the GDL pores. Thus, finding optimal values of the GDL parameters such as porosity, permeability and wettability are important issues in PEMFCs research [5–7].

Recently, a great deal of attention is given to the study of anisotropic characteristics of the GDL, i.e., permeabilities are different in the in-plane and in the through-plane directions. Measurements of through-plane permeability were performed [7,8], and the correlation between the through-plane permeability and the limiting current density was studied [9]. In addition, several studies [10–12] indicated that in-plane permeability is more relevant to PEMFCs performance, particularly for the serpentine flow

channel in which the cross-flow occurs due to pressure gradient between the neighbor channels. Feser et al. [13] and Gostick et al. [14] measured in-plane permeability of carbon paper and carbon cloth GDL as a function of compression ratio, and found that the permeability of the GDL decreased with the increase of the compression force.

Early work on simulation of fluid flow in the GDL used macroscopic models based on the volumetric averaging of conservation equations in an elementary volume assuming a homogeneous porous medium with a constant permeability, which were solved numerically by conventional CFD methods [15]. Recently, some work on the application of the lattice Boltzmann method (LBM) to study transport in GDL of PEMFCs have been carried out [16–18]. Using single-phase LBM approach, Wang and Afsharpoya [16] studied the 2D fluid flow though a section of serpentine channel and a channel filled or partially filled with porous medium with application to PEMFCs gas flow channel. Joshi et al. [17] used the LBM to model the mass transport of H_2 and the produced H_2O (vapor) in the presence of N_2 in the 2D porous anode structure of a solid oxide fuel cell (SOFC). Park and Matsubara [18] studied the gas flow through a fiber tow in the woven carbon cloth GDL by using a 3D LBM approach in solving the Stokes and Brinkman equations numerically in the void and in the porous tow, respectively. The LBM used in [18] is based on the Bhatnagar–Gross–Krook (BGK) model with a standard bounce-back boundary scheme for solid boundary condition. The BGK model, which has a single-relaxation-time (SRT) collision operator, suffers from numerical instability and viscosity dependence of flow when solid boundary is present [19]. The viscosity dependence problem becomes severe for simulating flow through porous media. To overcome these deficiencies, the multiple-relaxation-time (MRT) model has recently been developed [19–21], in which different relaxation times are used for different kinetic modes.

In this paper, the 3D micro-scale flow of liquid transport in the nonwoven carbon paper GDL is simulated using the MRT/LBM approach [19,20]. In-plane and through-plane permeabilities of the anisotropic GDL are simulated for several samples that are reconstructed using the stochastic method [22,23]. The samples with different porosities and microstructures are achieved to simulate different GDL compression and PTFE contents and the calculated permeabilities are compared with existing measurements [13]. The numerically obtained relationship between the permeability and the porosity is compared with the previously developed correlations and with fractal models [24,25].

2. Description of the simulation model

2.1. Multiple-relaxation-time LBM model

The MRT/LBM model transforms the distribution function in the velocity space of the SRT/LBM model to the moment space through a transformation matrix. Since moments of the distribution function directly represent physical quantities, the moment representation offers a convenient way to perform the relaxation collision processes with different relaxation times according to different time scales of various physical processes. In the SRT/LBM model, the evolution of the distribution function $f_\alpha(\mathbf{x}, t)$ is described by the following equation:

$$f_\alpha(\mathbf{r}+\mathbf{e}_\alpha\delta t, t+\delta t)-f_\alpha(\mathbf{r}, t)=\mathbf{S}\left[f_\alpha^{eq}(\mathbf{r}+\mathbf{e}_\alpha\delta t, t+\delta t)-f_\alpha(\mathbf{r}, t)\right]+F_\alpha \quad (1)$$

where $\mathbf{S}$ is the relaxation matrix [21], which is a diagonal matrix with same diagonal elements in SRT model; $\mathbf{e}_\alpha$ is lattice velocity in the αth direction and the corresponding lattice velocity directions are shown in Fig. 1. f_α^{eq} is the equilibrium distribution of f_α given as a function of density ρ and velocity $\mathbf{u}$:

$$f_\alpha^{eq} = w_\alpha\rho\left[1 + \frac{\mathbf{e}_\alpha\cdot\mathbf{u}}{c_s^2} + \frac{(\mathbf{e}_\alpha\cdot\mathbf{u})^2}{2c_s^4} - \frac{\mathbf{u}\cdot\mathbf{u}}{2c_s^2}\right]. \quad (2)$$

For the three-dimensions 19-velocity (3DQ19) model, the lattice velocity $\mathbf{e}_\alpha$ and the weight coefficients w_α are given as follows:

$$\mathbf{e}_\alpha = \begin{cases} (0, 0, 0), & \alpha=0; \\ (\pm1, 0, 0)c, \ (0, \pm1, 0)c, \ (0, 0\pm1)c, & \alpha=1, 2, \ldots, 6; \\ (\pm1, \pm1, 0)c, \ (\pm1, 0, \pm1)c, \ (0, \pm1, \pm1)c, & \alpha=7, 8, \ldots, 18. \end{cases}$$

$$w_\alpha = \begin{cases} 1/3, & \alpha = 0; \\ 1/18, & \alpha = 1, 2, \ldots, 6; \\ 1/36, & \alpha = 7, 8, \ldots, 18. \end{cases} \quad (3)$$

F_α in Eq. (1) represents the external force, which is given by [26]

$$F_\alpha = w_\alpha\left[\frac{\mathbf{e}_\alpha - \mathbf{u}}{c_s^2} + \frac{\mathbf{e}_\alpha\cdot\mathbf{u}}{c_s^4}\mathbf{e}_\alpha\right]\cdot\mathbf{F} \quad (4)$$
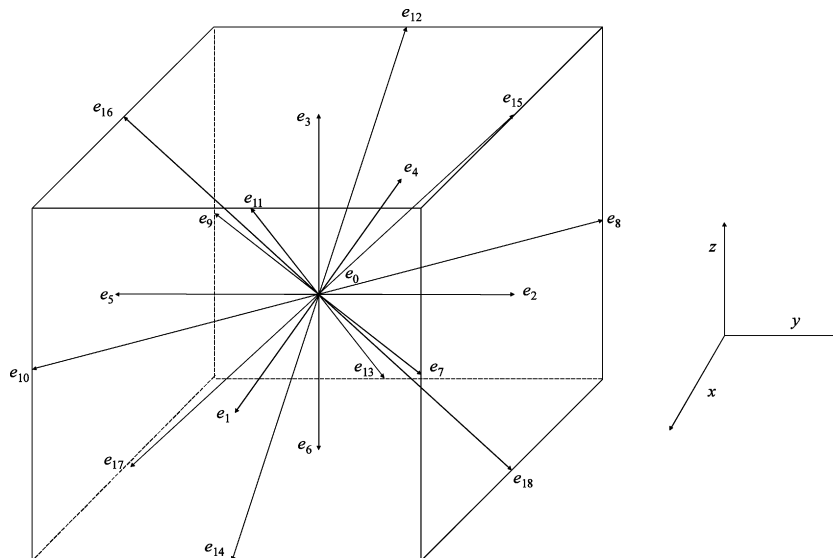

Fig. 1. Lattice velocity directions of the D3Q19 LBM.

where **F** is the external force and c_s is the speed of sound which is given by $c/\sqrt{3}$, where $c = \delta x/\delta t$ is the lattice speed and δx is the lattice distance.

By multiplying a transformation matrix **Q** in Eq. (1), the evolution function can be expressed in the moment space as

$$\mathbf{m}(\mathbf{r}+\mathbf{e}\delta t, t+\delta t)-\mathbf{m}(r, t)=\widehat{\mathbf{S}}\left[\mathbf{m}^{eq}(\mathbf{r}+\mathbf{e}\delta t, t+\delta t)-\mathbf{m}(\mathbf{r}, t)\right]+\mathbf{Q}\cdot\mathbf{F} \tag{5a}$$

where

$$\mathbf{m} = \mathbf{Q}\cdot\mathbf{f} \tag{5b}$$

and

$$\mathbf{m}^{eq} = \mathbf{Q}\cdot\mathbf{f}^{eq} \tag{5c}$$

are the vectors of the moments distribution function and its corresponding equilibrium moments vector, respectively. The transformation matrix **Q** is constructed such that the relaxation matrix $\widehat{\mathbf{S}}$ in moment space can be reduced to the diagonal form and is given in [20] for D3Q19 model. As a result, the diagonal relaxation matrix $\widehat{\mathbf{S}}$ in Eq. (5a) is

$$\widehat{\mathbf{S}} = \text{diag}(s_0, s_1, s_2, s_3, s_4, s_5, s_6, s_7, s_8, s_9, s_{10}, s_{11}, s_{12}, s_{13}, s_{14},$$
$$s_{15}, s_{16}, s_{17}, s_{18}) \tag{6}$$

where $s_0 = s_3 = s_5 = s_7 = 0$, $s_1 = s_2 = s_{9-15} = 1/\tau$, and $s_4 = s_6 = s_8 = s_{16-18} = 8((2-1/\tau)/(8-1/\tau))$ are propositional values in [19] and τ is related to the fluid viscosity ν by

$$\tau = \frac{3\nu}{\delta t + 0.5} \tag{7}$$

Additionally, the equilibrium moments $\mathbf{m}^{eq}$ are [19]:

$$\mathbf{m}_0^{eq} = \rho \tag{8a}$$

$$\mathbf{m}_1^{eq} = -11\rho + 19\frac{\boldsymbol{j}\cdot\boldsymbol{j}}{\rho_0} \tag{8b}$$

$$\mathbf{m}_2^{eq} = 3\rho - \frac{11}{2}\frac{\boldsymbol{j}\cdot\boldsymbol{j}}{\rho_0} \tag{8c}$$

$$\mathbf{m}_3^{eq} = j_x, \qquad \mathbf{m}_5^{eq} = j_y, \qquad \mathbf{m}_7^{eq} = j_z \tag{8d}$$

$$\mathbf{m}_4^{eq} = -\frac{2}{3}j_x, \qquad \mathbf{m}_6^{eq} = -\frac{2}{3}j_y, \qquad \mathbf{m}_8^{eq} = -\frac{2}{3}j_z \tag{8e}$$

$$\mathbf{m}_9^{eq} = \frac{3j_x^2 - \boldsymbol{j}\cdot\boldsymbol{j}}{\rho_0}, \qquad \mathbf{m}_{10}^{eq} = -\frac{3j_x^2 - \boldsymbol{j}\cdot\boldsymbol{j}}{2\rho_0} \tag{8f}$$

$$\mathbf{m}_{11}^{eq} = \frac{j_y^2 - j_z^2}{\rho_0}, \qquad \mathbf{m}_{12}^{eq} = -\frac{j_y^2 - j_z^2}{2\rho_0} \tag{8g}$$

$$\mathbf{m}_{13}^{eq} = \frac{j_x j_y}{\rho_0}, \qquad \mathbf{m}_{14}^{eq} = \frac{j_y j_z}{\rho_0}, \qquad \mathbf{m}_{15}^{eq} = \frac{j_x j_z}{\rho_0} \tag{8h}$$

$$\mathbf{m}_{16}^{eq} = \mathbf{m}_{17}^{eq} = \mathbf{m}_{18}^{eq} = 0 \tag{8i}$$

where ρ_0 is the mean density of the fluid which is used to reduce compressibility effects in the model [19,20].

The macroscopic local density $\rho(\mathbf{x}, t)$ and the momentum $\mathbf{j}(\mathbf{x}, t)$ are obtained as

$$\rho = \sum_{\alpha=0}^{18} f_\alpha \tag{9a}$$

$$\mathbf{j} = \rho_0\mathbf{u} = \sum_{\alpha=0}^{18} f_\alpha\mathbf{e}_\alpha + \frac{\delta t}{2}\mathbf{F} \tag{9b}$$

Employing the Chapman–Enskog multiscale analysis for D3Q19 model, Eqs. (1) and (5) can lead to the Navier–Stokes equations under the low Mach number limitation:

$$\frac{\partial\rho}{\partial t} + \nabla\cdot(\rho\mathbf{u}) = 0 \tag{10a}$$

$$\frac{\partial(\rho\mathbf{u})}{\partial t} + \nabla\cdot(\rho\mathbf{uu}) = -\nabla(c_s^2\rho) + \nabla\cdot(\rho\nu\nabla\mathbf{u}) + \mathbf{F} \tag{10b}$$

where the pressure is given by $p = c_s^2\rho$.

2.2. Boundary conditions

Since the methods developed in the SRT model for boundary conditions are still applicable in the MRT approach, the moment distribution function **m** in the MRT model is transformed to the distribution function **f** in the velocity space by

$$\mathbf{f} = \mathbf{Q}^{-1}\mathbf{m} \tag{11}$$

when dealing with the boundary conditions.

2.2.1. Inlet/outlet boundary

The velocity and pressure boundary conditions at the inlet and outlet are dealt with using the bounce-back of the non-equilibrium distribution rule [27]. For the D3Q19 model, for example, if the inlet boundary face is perpendicular to the x-direction with the lattice velocity e_1, e_7, e_{10}, e_{11} and e_{14} (as shown in Fig. 1) pointing into the calculation region, the distribution functions f_1, f_7, f_{10}, f_{11} and f_{14} in these directions are unknown after streaming. These unknown distribution functions are determined by the rest of the known distribution functions in order to satisfy the specified boundary conditions.

According to Eqs. (9a) and (9b), the unknown distribution function $f_i(i = 1, 7, 10, 11, 14)$ at the inlet boundary satisfy the equations as follow:

$$f_1 + f_7 + f_{10} + f_{11} + f_{14} = \rho_{in} - (f_0 + f_2 + f_3 + f_4 + f_5 + f_6 + f_8 + f_9$$
$$+ f_{12} + f_{13} + f_{15} + f_{16} + f_{17} + f_{18}) \tag{12a}$$

$$f_1 + f_7 + f_{10} + f_{11} + f_{14} = \rho_{in}\frac{u_x}{c} + (f_4 + f_8 + f_9 + f_{12} + f_{13}) \tag{12b}$$

where the inlet density ρ_{in} can be obtained by equating the right-hand side of Eq. (12a) to the right-hand side of Eq. (12b) to give:

$$\rho_{in} = \frac{E}{1 - u_x/c} \tag{13a}$$

where

$$E = (f_0 + f_2 + f_3 + f_5 + f_6 + f_{15} + f_{16} + f_{17} + f_{18} + 2(f_4 + f_8 + f_9$$
$$+ f_{12} + f_{13}) \tag{13b}$$

To close the system of equations, the bounce-back rule for the non-equilibrium part of the distribution functions $f_i(i = 1, 7, 10, 11, 14)$ is applied

$$f_i = f_i^{eq} + (f_{i'} - f_{i'}^{eq}) \tag{14}$$

with f_i^{eq} calculated from ρ_{in} given by Eq. (13) and with i' denotes the opposite lattice velocity of i, that is $e_i = -e_{i'}$. Eqs. (12) and (14) are sufficient to determine all the unknown f_i. However, in order to keep the correct y- and z-direction momenta, these distribution functions are modified as follows [27]:

$$f^* = \frac{f_i - (j_y e_{iy} + j_z e_{iz})}{2}, \quad i = 1, 7, 10, 11, 14 \tag{15}$$

where $j_y = \sum_{\alpha=0}^{18} f_\alpha\mathbf{e}_{\alpha y}$ and $j_z = \sum_{\alpha=0}^{18} f_\alpha\mathbf{e}_{\alpha z}$.

Similarly, when the boundary pressure (density) is specified, the x-direction velocity can also be determined by Eq. (12), i.e.,

$$u_x = c \left[1 - \frac{E}{\rho_{in}} \right] \qquad (16)$$

Under the assumption that velocities in y- and z-directions are zero on the boundary, the unknown distribution functions $f_i(i = 1, 7, 10, 11, 14)$ can be obtained using Eqs. (14) and (15) as the same as velocity boundary.

2.2.2. Solid boundary

The no-slip condition on the solid boundary can be approximated using the standard bounce-back boundary conditions, in which the liquid particles reflect their directions when colliding with the solid wall. However, it has been demonstrated that the multi-reflection (MR) boundary, which was developed originally for solving moving solid boundary problems, is much more accurate than bounce-back rule, especially for porous media flow [19,20]. In addition, the MR boundary condition utilizes some moment space parameters, which can be directly obtained in the MRT/LBM model.

After the streaming process, the distribution function out of the solid is constructed in MR boundary condition as follows:

$$f_{i'}(\mathbf{x}, t) = k_1 f_i(\mathbf{x} + \mathbf{e}_i \delta t, t) + k_2 f_i(\mathbf{x}, t) + k_3 f_i(\mathbf{x} - \mathbf{e}_i \delta t, t) + k_4 f_{i'}(\mathbf{x}, t)$$
$$+ k_5 f_{i'}(\mathbf{x} - \mathbf{e}_i \delta t, t) + k_6 N_{i'}(\mathbf{x}, t)/\nu \qquad (17)$$

with the coefficients k_j ($j = 1$–6) being functions of the solid boundary location given by [19]

$$k_1 = 1, \qquad k_2 = -k_4 = \frac{1 - 2q - 2q^2}{(1 + q)^2}, \qquad k_3 = -k_5 = \frac{q^2}{(1 + q)^2},$$
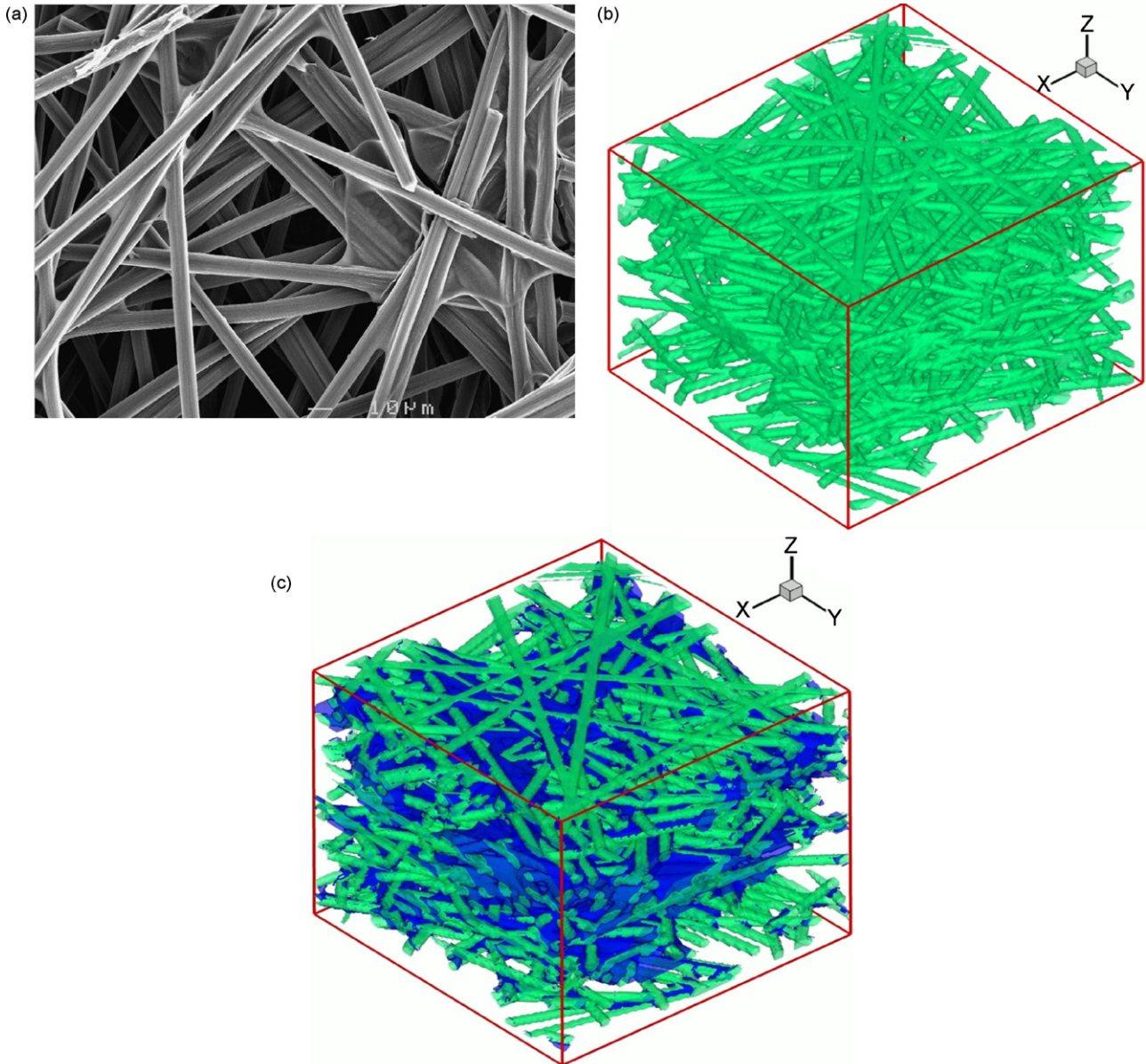
$$k_6 = \frac{1}{4(1 + q)^2}.$$

Fig. 2. Micrographs of the carbon paper GDL. (a) SEM image of the Toray 060 GDL. (b) 3D geometer of the reconstructed carbon paper GDL. (c) 3D geometer of the reconstructed carbon paper GDL with 15% PTFE content.

where q is defined as the ratio of the distance between the first fluid node near the wall and the solid wall to the lattice distance. In Eq. (17) the quantity N is the non-equilibrium term relating to moments distribution functions **m** and can be calculated as

$$\mathbf{N} = \mathbf{M}^{-1} \cdot \hat{\mathbf{S}} \cdot (\mathbf{t}^{eq} - \mathbf{t}) \qquad (18a)$$

where $\mathbf{t} = (0, 0, 0, 0, m_4, 0, m_6, 0, m_8, 0, ..., 0, m_{16}, m_{17}, m_{18})^{\mathrm{T}}$ is a vector, having partial elements of the moments **m**, and

$$\mathbf{t}^{eq} = (0, 0, 0, 0, m_4^{eq}, 0, m_6^{eq}, 0, m_8^{eq}, 0, ..., 0, m_{16}^{eq}, m_{17}^{eq}, m_{18}^{eq})^{\mathrm{T}} \quad (18b)$$

The main steps, when applying the MRT/LBM model described above, can be summarized as follows:

1. Calculating the equilibrium moments $\mathbf{m}^{eq}$ from Eq. (8);
2. Evolution of the moments distribution function according to Eq. (5);
3. Transforming the moment distribution function **m** to the velocity distribution function **f** by Eq. (11);
4. Implementing the streaming process using the velocity distribution function **f** and imposing the boundary condition from Eqs. (12)–(18);
5. Updating the local density $\rho(\mathbf{x}, t)$ and the local velocity $\mathbf{u}(\mathbf{x}, t)$ according to Eq. (9).

2.3. Reconstruction of carbon paper GDL

The reconstruction of 3D porous media can be obtained by two methods: the 3D imaging combination and the virtual stochastic generation. The former employs the 3D images of the porous medium scanned by X-ray or scanning laser microscopy and then integrates them to achieve the geometry construction. The later reconstructs the porous medium microstructure based on the statistical information of the porous medium. The low cost and easy implementation of geometry generation make the stochastic generation method a better choice than the imaging combination method [22]. In the present study, the method proposed by Schladitz et al. [23] based on the stochastic generation method is adopted to reconstruct the carbon paper GDL.

Fig. 2(a) presents the SEM image of the Toray 060 carbon paper. In general, an actual carbon paper GDL consists of carbon fibers, randomly oriented in a plane, leading to different in-plane and through-plane properties. Since the reconstruction of the real GDL is difficult, some assumptions are made for simplification: (i) carbon fibers in GDL are cylinders having a fixed and uniform diameter; (ii) fibers are straight and infinitely long; (iii) fibers are allowed to overlap. In addition, according to fabrication process of carbon paper, the fibers in the material plane are stochastic arranged, thus this plane can be considered to be isotropic, and fibers oriented to the direction of the GDL thickness can be neglected. Giving the GDL size, porosity and fiber diameter D, the reconstruction of carbon paper is achieved by placing the fibers in a plane with arbitrary positions and orientations one layer by one layer. It should be noted that the porosity of the reconstructed GDL is achieved in this process by making sure the porosity in each layer approximately equal to the prescribed value. Thus, although the final porosity is not exactly equal to the prescribed value, but is an acceptable approximation. Fig. 2(b) shows the microstructure of the reconstructed carbon paper GDL with the size of $150 \times 150 \times 127$ lattice grid and a prescribed porosity of 0.791, where x or y is the in-plane direction and z the through-plane direction. This sample is also considered as the original sample without compression and PTFE in the following study.

The compressed samples are reconstructed under the assumption that the compression process only change the thickness of the original samples and does not change the fibers shape. Thus, the reconstruction process is the same as mentioned above, only with different porosities and thicknesses according to different compression ratios. The relationship between the compression ratio r and the porosity ϕ can be expressed as [13]

$$\phi = 1 - \frac{1 - \phi_0}{1 - r} \qquad (19)$$

where ϕ_0 is the uncompressed GDL porosity, and $r = (h_0 - h)/h_0$ is defined as the change of the thickness $h_0 - h$ after compression divided by the uncompressed thickness h_0. Thus, $r = 0$ means no compression.

If the PTFE is added on the carbon paper GDL, one more step is added after the fiber GDL generation: the pore volume close to the fiber in the sample is randomly filled by the PTFE. This process is repeated until the prescribed PTFE content is achieved. Thus, the pores surrounding by more fibers will have more probability to fill with PTFE. Fig. 2(c) shows the geometry of the reconstructed GDL with 15% PTFE content and the same size of $150 \times 150 \times 127$ lattice grid. The final porosity ϕ can be expressed approximately as a function of PTFE content w to give:

$$\phi = \phi_0 - a \frac{w(1 - \phi_0)}{1 - w} \qquad (20)$$

where ϕ_0 is the original porosity before PTFE is added, and $a = 0.9$ is the density ratio of the carbon fiber and the PTFE [7].

3. Model validation

To validate the present model, two examples of single-phase flow will be simulated: (i) fully-developed flow in a rectangular channel and (ii) flow through body-centered arrays of spheres. For the first problem, it is noted that the analytical solution of the velocity profile in a fully-developed flow in a channel with a rectangular cross section having width $2a$ and height $2b$ is [28]

$$V(x, y) = V_0 \left[1 - \left(\frac{y}{b} \right)^2 + 4 \sum_{i=1}^{\infty} \frac{\cosh(\beta_i x/b) \cos(\beta_i y/b)}{\cosh(\beta_i a/b)} \right] \qquad (21)$$

with $V_0 = b^2 \Delta p/(2\eta L)$ and $\beta_i = (2i - 1)\pi/2$, $i = 1, 2, ..., n$, where Δp is the pressure drop over the channel length L, and η is the dynamic viscosity of the fluid. Fig. 3(a) shows the comparison of velocity profile along center line of the longer side obtained from the analytical solution given by Eq. (21) with prescribed pressure gradient $\Delta p/L = 7.5 \times 10^{-3}$ and $\eta = 17.5$, and the LBM simulation for two rectangular channels with the cross section size of 60×30 and 80×30, respectively. It is clearly shown that the simulation results are in excellent agreement with the analytical solution. The corresponding pressure drop along the channel is presented in Fig. 3(b) which shows that the average pressure drops linearly along the channel length.

The validation of the permeability for flow through body-centered cubic arrays of spheres will be considered next. In LBM simulation, the permeability k of the porous medium can be calculated according to Darcy's law under the low Reynolds number condition

$$\mathbf{u}_d = \frac{k}{\eta} (\nabla p + \mathbf{F}) \qquad (22)$$

where $\mathbf{u}_d$ is the Darcy velocity as the superficial velocity of the fluid and **F** is the body force acting on the fluid. The permeability k is generally described in terms of the porosity ϕ. The Kozeny–Carman (KC) equation is the most widely used semi-empirical relationship,
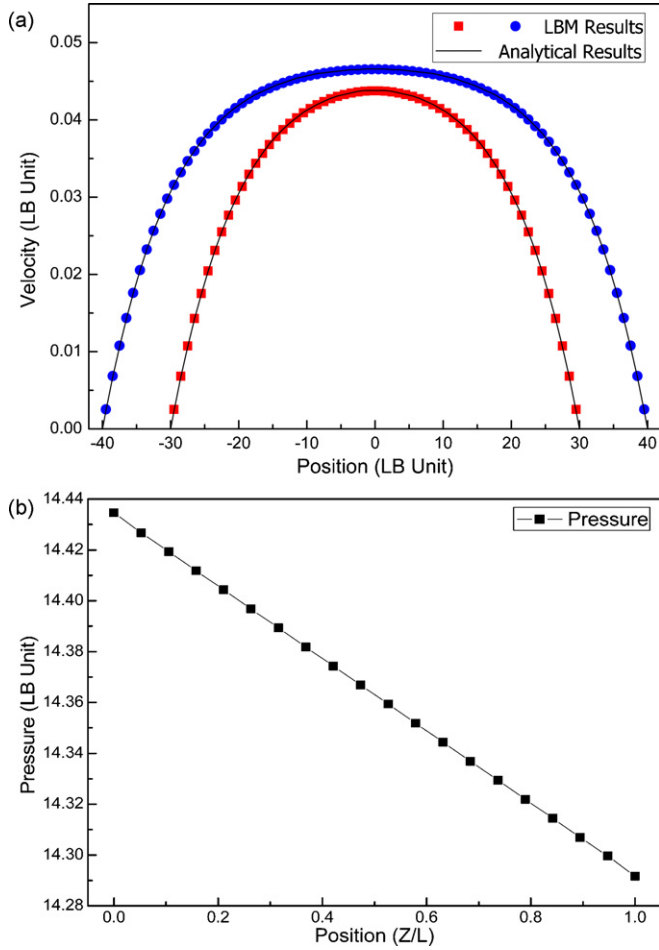
Fig. 3. Comparison of the LBM simulation results with the analytical solution (solid line) for velocity profile of fully-developed flow along the centerline of the longer side in two rectangular channels. (a) Flow profile along the centerline of the longer side in rectangular channels (with cross sections: (■) 60×30; (●) 80×30). (b) Pressure drop along the channel.

given by

$$k = C \frac{\phi^3}{(1-\phi)^2} \tag{23}$$

where C is the Kozeny–Carman constant and $C = d^2/180$ has been used for packed-spheres porous media with sphere diameter d.

Fig. 4 shows the comparison of simulation results of the dimensionless permeability k/d^2 in the packed sphere porous medium with the analytical solutions given by Zick and Homsy [29] and the KC relation given by Eq. (23). It can be seen that the LBM simulation results are in good agreement with the analytical solution for the whole range of ϕ, but the KC relation shows large error as the porosity increases because the KC equation was determined empirically for densely packed spheres with small value of ϕ.

After this validation, the viscosity effect on the permeability will now be compared based on the MRT and BGK models for the reconstructed carbon paper GDL (as shown in Fig. 2(b)) with the average porosity of 0.791. Fig. 5 shows that the dimensionless permeabilities k/D^2 calculated by the MRT model are constant for various viscosities, while the permeability calculated in BGK model is significantly increased with the increase of viscosity. Therefore, the results from the present MRT model do not suffer from the problem
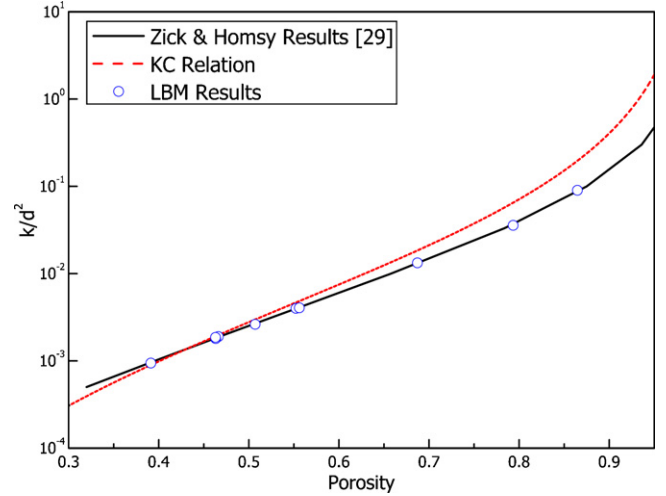
Fig. 4. Comparison of the LBM simulated permeability with the analytical solution and the KC relation for body-centered cubic spheres arrays.

of viscosity dependent permeability, and is capable of simulating single-phase flow through porous media more accurately.

4. Results and discussion

In the LBM model, the simulation parameters are in terms of the lattice units that do not have physical units. To relate the physical space with lattice space, a length scale l_0, a time scale t_0 and a mass scale m_0 should be chosen such as $l_0 = 1.5 \times 10^{-6}$ m, $t_0 = 5.0 \times 10^{-7}$ s, and $m_0 = 5.0 \times 10^{-17}$ kg in present study. As a result, the physical parameters of velocity u_p, pressure p_p, and permeability k_p can be calculated from the quantities in lattice system (subscripted by L) and the scale parameters as follows:

$$u_p = u_L \frac{l_0}{t_0}, \qquad p_p = p_L \frac{m_0}{l_0 t_0^2}, \qquad k_p = k_L l_0^2 \tag{24}$$

For the reconstructed carbon paper GDL, the fiber diameter of 7.5 μm is prescribed. In order to reduce the influence of the fiber on the inlet/outlet boundary, five more lattices are added between the GDL and inlet/outlet boundary. For in-plane flow, pressure boundaries are specified on the inlet and outlet, respectively (perpendicular faces to x-direction in Fig. 2(b)), and two
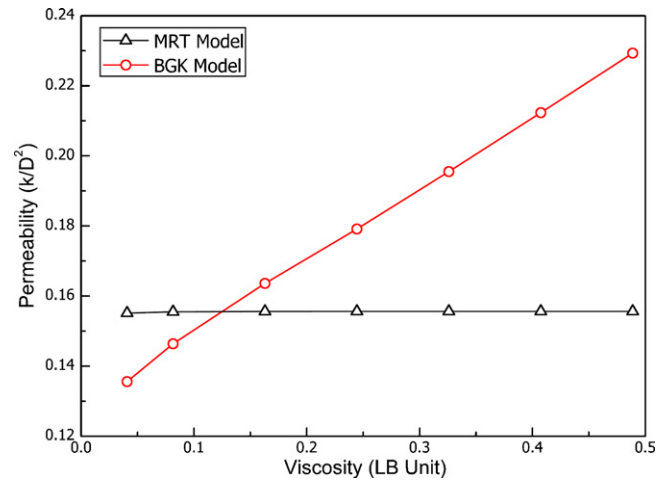

Fig. 5. Comparison of the permeability computed based on MRT/LBM and BGK/LBM models with various viscosities.
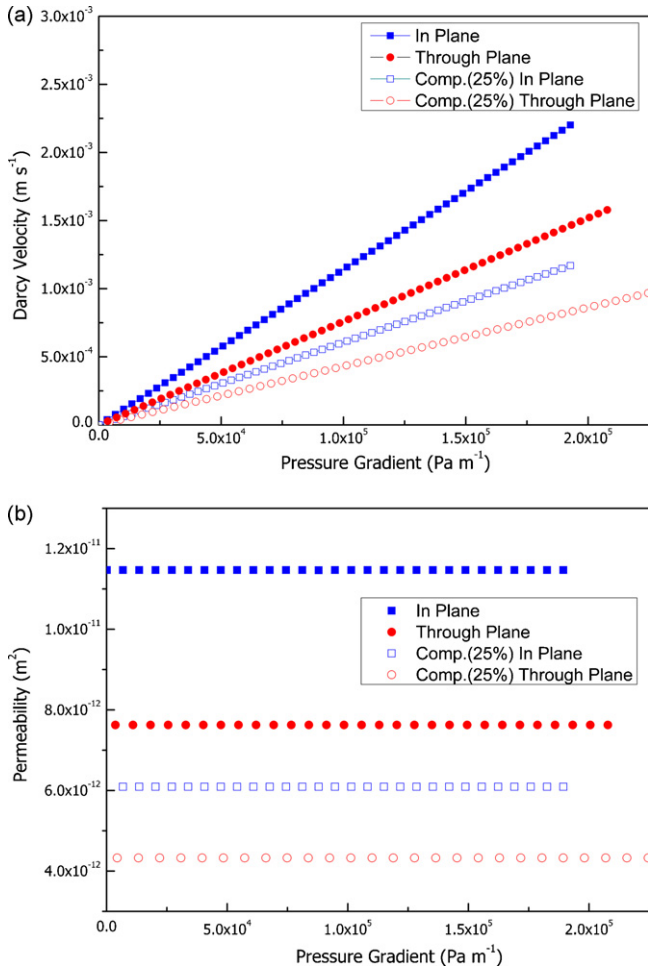
Fig. 6. Darcy velocity and permeability as a function of pressure gradient in uncompressed and compressed carbon papers. (a) Darcy velocity vs. pressure gradient. (b) Permeability at different pressure gradient.

solid boundaries are specified on the top and bottom surfaces (perpendicular faces to z-direction in Fig. 2(b)), keeping the others periodic boundary conditions. For through-plane flow, except for the pressure boundaries condition on the inlet and outlet (perpendicular faces to z-direction in Fig. 2(b)), the rest four faces are all specified to be periodic boundary. Additionally, the reproducibility of the reconstructed GDL must be ensured. In the present study, with the GDL size of $150 \times 150 \times 127$ lattice and the length scale of $1.5\,\mu m$, the GDLs are firstly reconstructed four times with the same porosity. The differences among the calculated permeability of the four GDLs are less than 5%, so the reconstructed GDL size ($150 \times 150 \times 127$ lattice) can meet the requirement of reproducibility, and the corresponding GDL thickness is $190.5\,\mu m$ (i.e., $127 \times 1.5\,\mu m$), which is the same as the Tory 060 carbon paper GDL.

Fig. 6(a) shows the relationship between the Darcy velocity and the pressure gradient for the original and 25% compressed GDL based on MRT/LBM simulation. It clearly shows that the Darcy velocity is linearly proportional to the pressure gradient for both in-plane and through-plane flows within the calculated pressure gradient bound, and the corresponding permeability is almost constant with pressure gradient as shown in Fig. 6(b). Therefore, it can be said that the Darcy law is valid and the inertial force can be neglected in flow through carbon paper GDL if the pressure gradient does not exceed the bound in this study.

4.1. Velocity, streamline and pressure distribution

Fig. 7 shows the 3D distribution of velocity, streamline and pressure in the carbon paper GDL obtained from the present MRT/LBM model. It is seen that the flow field in GDL is quite complicated for both in-plane and through-plane due to the complicated structure of the GDL. In each slices, the magnitude of the velocity greatly depends on location of the void space. It can be seen from these graphs that the main flow path is through larger pores because of their small flow resistance, and it can be expected that the pressure would drop rapidly at the locations containing dense fibers.

4.2. Permeability

It is observed from Fig. 7 that the streamlines in through-plane flow are a little more tortuous than in-plane flow. This implies that liquid particles in through-plane flow will detour more obstacles resulting in larger flow resistance. Thus, the in-plane permeability always has a larger value than through-plane in a given carbon paper GDL as shown in Fig. 8.

4.2.1. Effects of compression

The effects of compression ratio (r) on in-plane and through-plane permeabilities of carbon papers are shown in Fig. 8, where the in-plane permeability of Tory 060 obtained by Feser et al. [13] and the through-plane permeability of Tory 090 obtained by Gostick et al. [30] are also plotted for comparison purposes. The in-plane permeability obtained by the present model agrees well with measurements by Feser et al. [13], with the divergence less than 15% in the whole range of compression ratio. On the other hand, no measurements are available in literature for the through-plane permeability under compression. However, Gostick et al. [30] measured the through-plane permeability for uncompressed Toray 090 to be $8.3 \times 10^{-12}\,m^2$ while Mathias et al. [7] measured the through-plane permeability of uncompressed Toray 060 to be approximately in the range of 5–$10 \times 10^{-12}\,m^2$. The simulated value of $7.62541 \times 10^{-12}\,m^2$ (with no compression for $r = 0$) falls in the middle of these values.

In practice, it is more convenient to describe the permeability as a function of porosity, such as KC relation given by Eq. (23). Since the KC relation was originally determined for granular porous media and is applicable only for low porosity materials (as shown in Fig. 4), therefore, the KC relation does not always predict the correct permeability for fibrous media [31], which is similar to carbon paper GDL with high porosities. However, Feser et al. [13] found that KC relation can accurately describe the permeability of carbon paper in a narrow porosity range by fitting a proper Kozeny–Carman constant C. On the other hand, Tomadakis and Robertson [32] suggested that the permeability–porosity KC relationship (Eq. (23)) of carbon paper (which has randomly overlapping fiber structure) should be replaced by

$$k = C \frac{\phi}{(\ln \phi)^2} \tag{25}$$

Tomadakis and Robertson [32] also proposed a more comprehensive relation to predict the anisotropic permeability of in-plane and through-plane, based on the Λ-base method of Johnson et al. [33]. For randomly overlapping fiber structures, the Λ-base relation is described as [32]

$$k = R^2 \frac{\phi(\phi - \phi_p)^{\alpha+2}}{8 \ln^2 \phi (1 - \phi)^\alpha [(\alpha + 1)\phi - \phi_p]^2} \tag{26}$$

where R is the radius of the fiber, ϕ_p the percolation threshold and α a constant depending on the structure and the flow direction.
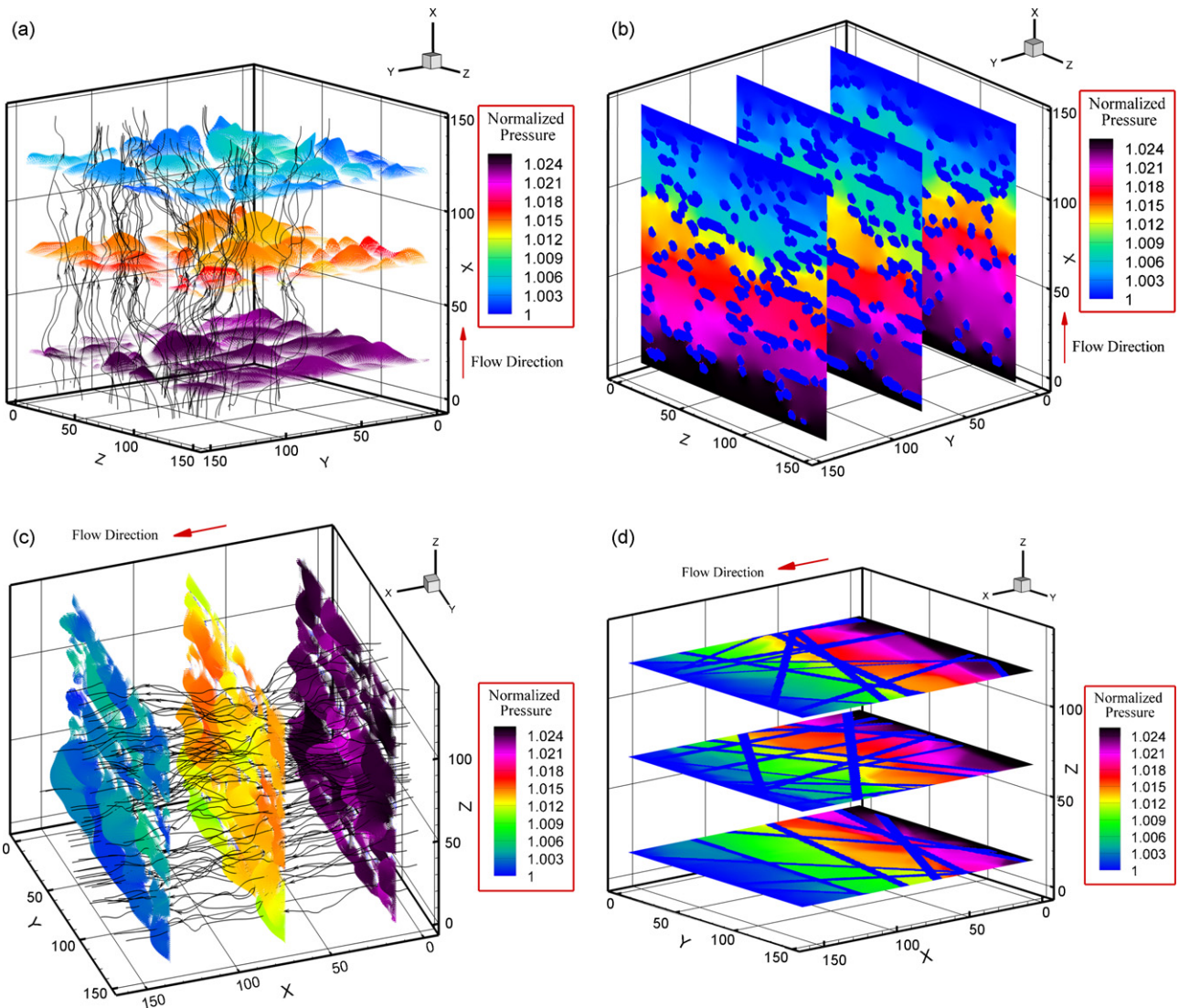
Fig. 7. Lattice Boltzmann simulation results for single-phase flow through 3D carbon paper GDL (pressure is normalized to the outlet pressure). (a) Velocity and streamline for through-plane flow. (b) Pressure contous for through-plane flow. (c) Velocity and streamline for in-plane flow. (d) Pressure contous for in-plane flow.

Tomadakis and Robertson [32] found that for in-plane and through-plane flow in carbon paper where the percolation threshold ϕ_p is 0.11, the constants α in Eq. (26) are 0.521 and 0.785, respectively. Gostick et al. [14] found that Eq. (26) with $\alpha = 0.521$ fitted the in-plane permeability data of their carbon paper with fiber diameter of 9.2 μm very well.

Fig. 9 shows a comparison of the simulated in-plane and through-plane permeabilities of carbon paper with fiber diameter of 7.5 μm as a function of porosity with the predicted results from the relation given by Eq. (25) and Λ-base relation given by Eq. (26). For Eq. (25), the fitted constants C are 8.9504×10^{-13} and 6.2805×10^{-13} for in-plane and through-plane, respectively. From the figure, it is shown that Eq. (25) for both in-plane and through-plane permeabilities match with the simulated results very well. On the other hand, the Λ-base relation is shown to underestimate the simulated permeability by 35%, although it correctly predicts the trend of permeability as a function of porosity.

4.2.2. Effects of PTFE content

Following the method discussed in Section 2.3, several GDL samples with different PFTE contents are reconstructed. The simulated in-plane and through-plane permeabilities are presented as a
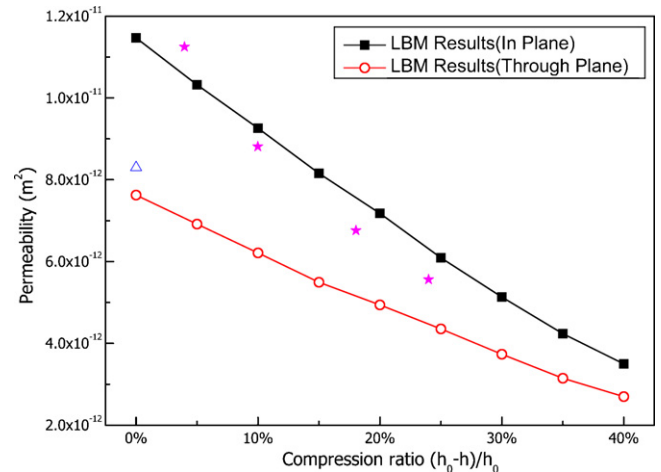

Fig. 8. Comparison of in-plane and through-plane permeabilities with measurements: (★) Feser et al. [13]; (△) Gostick et al. [30].
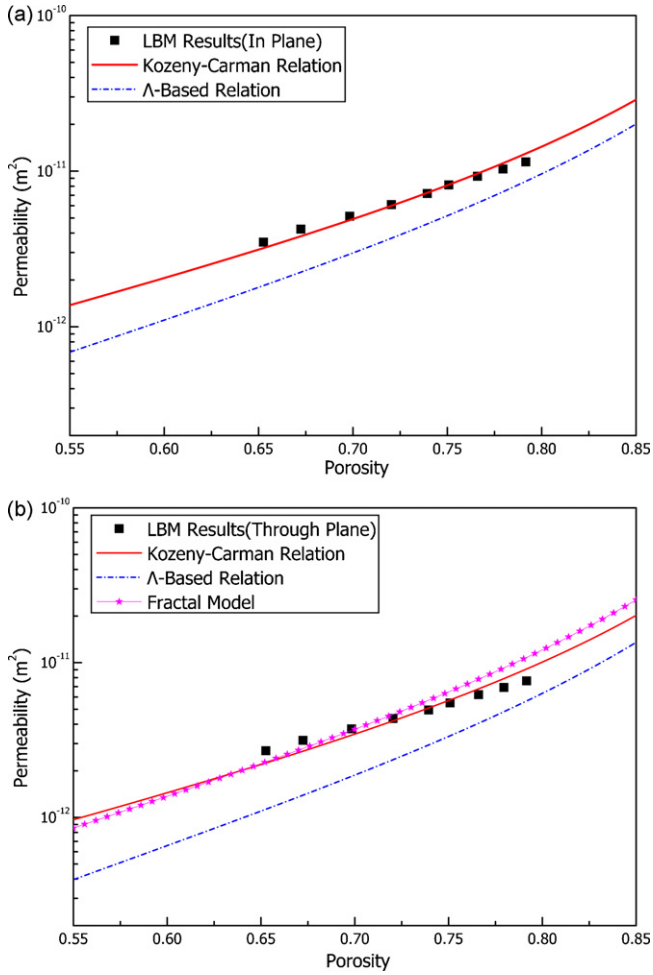
Fig. 9. Comparison of the LBM simulated in-plane and through-plane permeabilities with predictions from Eqs. (25) and (26). (a) In-plane; (b) through-plane.

function of porosity in Fig. 10. However, the simulated permeabilities do not fit Eq. (25) nor the Λ-base relation Eq. (26) very well and therefore are not presented. This may be attributed to the more complicated structural changes after the PTFE is added. It is obvious
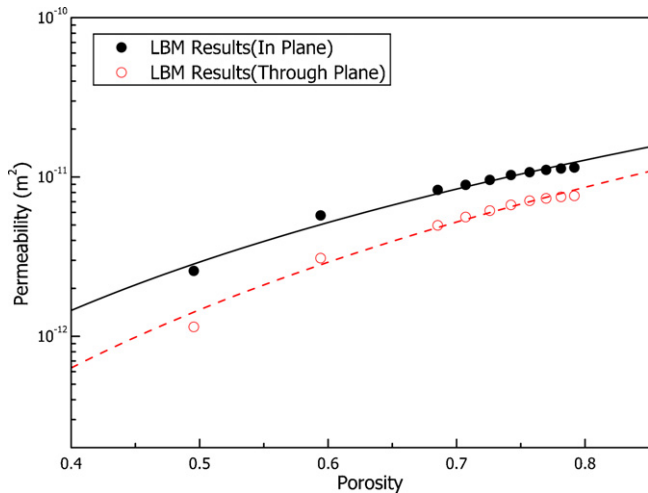

Fig. 10. Comparison of the simulation permeability with predictions from Eq. (27). Solid line for in-plane permeability with $C = 2.0$ and $a = 3.7681$. Dashed line for through-plane permeability with $C = 2.57$ and $a = 3.1355$.

from Fig. 2(c) that the carbon paper is not a pure fibrous structure with PTFE added due to the formation of PTFE films and blocks between the fibers. Therefore, a more general empirical formula [34] is used to fit the simulated results:

$$k = C\phi^a \tag{27}$$

where C and a are two constants. It is shown from Fig. 10 that Eq. (27) with the fitting values of $C = 2.0$ and $a = 3.7681$ for in-plane and $C = 2.57$ and $a = 3.1355$ for through-plane, matches with simulated values well.

4.3. Tortuosity

Generally, tortuosity is defined as the ratio of the flow path length to the thickness of the porous media along the flow direction. It is used to calculate the effective diffusivity controlling the mass transfer ability of reactant in GDL. The Bruggeman equation [14] has been commonly used for tortuosity prediction in PEMFC models, which is given by

$$\tau = \frac{1}{\phi^{0.5}} \tag{28}$$

However, Bruggeman equation was determined empirically from isotropic porous media, and therefore does not reflect the anisotropic property of carbon paper GDL. Koponen et al. [35] proposed the following formula for in-plane and through-plane tortuosity as

$$\tau = 1 + a\frac{1-\phi}{(\phi - \phi_p)^m} \tag{29}$$

where ϕ_p is the percolation threshold while a and m are constants.

We now compute the tortuosity of the carbon paper GDL after the flow field has been determined using the MRT/LBM model. For this purpose, two alternatives can be used to obtain the tortuosity by computing flow path lengths numerically. One may average over the actual lengths of the flow lines themselves, and the other may average the flow lines weighted by flux. The first alternative is suitable for molecular diffusion while the latter alternative is more natural for fluid flow in porous media. Both of these tortuosities of GDL can be calculated based on the following definition formulas [36]:

$$\tau_1 = \frac{(1/N)\sum_{i=1}^{N} l(\mathbf{r}_i)}{L} \tag{30a}$$

$$\tau_2 = \frac{\sum_{i=1}^{N}(l(\mathbf{r}_i)/L)u(\mathbf{r}_i)}{\sum_{i=1}^{N} u(\mathbf{r}_i)} \tag{30b}$$

where $N = 1000$ is the number of the streamlines used for average; $l(\mathbf{r}_i)$ is the length of the streamline starting at $\mathbf{r}_i$; L is the thickness of the porous media along the flow direction; $u(\mathbf{r}_i)$ is the tangential velocity at the starting point $\mathbf{r}_i$; τ_1 is the direct average tortuosity; τ_2 is the flux-weighted tortuosity. The simulated values of in-plane and through-plane tortuosities are shown in Fig. 11 as a function of porosity. It can be seen that (i) the value of tortuosity τ_1 is almost the same as tortuosity τ_2, although τ_1 is slightly larger especially at low porosity. This may be due to the narrow range of the streamline length at high porosity of GDL. (ii) The through-plane tortuosity is higher than in-plane (also seen in Fig. 7), and (iii) the Bruggeman equation (represented by a solid line) falls between the simulated in-plane and through-plane tortuosities. Matching Eq. (29) with the simulated tortuosities gives $a = 0.326$ and $m = 0.863$ for in-plane flow and $a = 0.714$ and $m = 0.543$ for through-plane flow, which was obtained based on the percolation threshold of 0.11 for carbon paper [32].
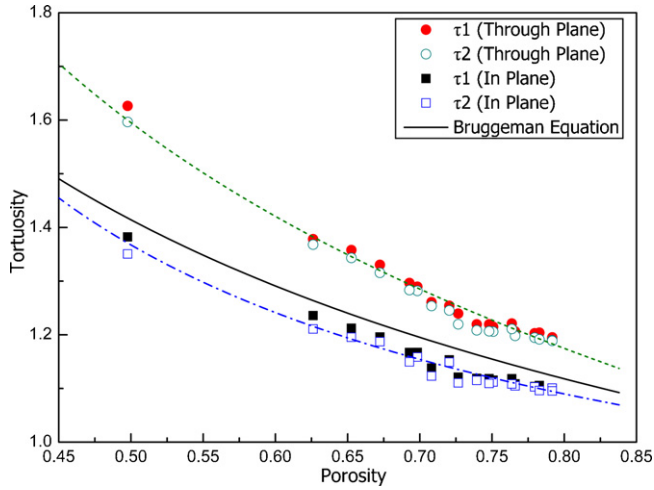
Fig. 11. The calculated tortuosity (Eq. (29)) as a function of porosity. Short dashed line is fitted to the calculated through-plane points by Eq. (30) with $a = 0.714$ and $m = 0.543$. Dashed dot line is fitted to the calculated in-plane points by Eq. (30) with $a = 0.326$ and $m = 0.863$. Solid line represents the Bruggeman equation (Eq. (28)).

4.4. Fractal model for permeability prediction

The fractal theory, as a useful tool to characterize irregular or disordered objects, has been applied to predict the permeability of porous media and GDL [37–39]. In these studies, the through-plane permeability is expressed as a function of area fractal dimension Df and tortuosity fractal dimension Dt, which are rather difficult to be determined using the box-counting method by analyzing SEM images of the GDL.

In this section, the fractal model will be used to predict the permeability of carbon paper GDL using the relationship of tortuosity and porosity obtained in Section 4.3. Yu and Li [38] have proposed a relationship between porosity and area fractal dimension Df as

$$\phi = \left(\frac{\lambda_{\min}}{\lambda_{\max}} \right)^{d_E - Df} \tag{31}$$

where d_E is Euclid dimension; $\lambda_{\min}$ and $\lambda_{\max}$ are the minimum and maximum pore sizes in GDL with their ratio assumed to be 10^{-2} in the following study.

The permeability of GDL based on fractal model [37,39] can be expressed as follows:

$$k = \frac{\pi L_0^{1-Dt} \lambda_{\max}^{3+Dt}}{128 A} \frac{Df}{3 + Dt - Df} \tag{32}$$

where L_0 is the representative length along the flow direction and A is the section area perpendicular to flow direction which can be written as [39]

$$A = \frac{\pi \lambda_{\max}^2 \left[1 - \left(\lambda_{\min}/\lambda_{\max} \right)^{2-Df} \right]}{4\phi} \frac{Df}{2 - Df} \tag{33}$$

Substituting Eqs. (33) and (31) with $d_E = 2$ into Eq. (32) gives

$$k = \frac{L_0^{1-Dt} \lambda_{\max}^{1+Dt}}{32} \left[\frac{2 - Df}{3 + Dt - Df} \right] \frac{\phi}{1 - \phi} \tag{34}$$

On the other hand, the flux-weighted tortuosity in fractal model can be obtained as follows:

$$\tau = \frac{\int_{\lambda_{\min}}^{\lambda_{\max}} (L(\lambda)/L_0) q(\lambda) f(\lambda) \, d\lambda}{\int_{\lambda_{\min}}^{\lambda_{\max}} q(\lambda) f(\lambda) \, d\lambda} = \frac{3 + Dt - Df}{4 - Df} \left(\frac{L_0}{\lambda_{\max}} \right)^{Dt-1} \tag{35}$$

where $f(\lambda) = Df \lambda_{\min}^{Df} \lambda^{-(Df+1)}$ is the pore number probability density with diameter λ; $q(\lambda) = (\pi \Delta p / 128 \mu L(\lambda)) \lambda^4$ is the flow rate through a capillary tube of diameter λ; $L(\lambda) = L_0 \lambda^{1-Dt}$ bases on the fractal theory.

Combining Eqs. (34) and (35), the tortuosity fractal dimension Dt disappears, thus the permeability can be expressed in terms of the tortuosity as

$$k = \frac{\lambda_{\max}^2}{32\tau} \frac{2 - Df}{4 - Df} \frac{\phi}{1 - \phi} \tag{36}$$

where the maximum pore size $\lambda_{\max}$ can be estimated for the regular fiber structure for through-plane flow [37]:

$$\lambda_{\max} = \sqrt{\frac{4\phi}{\pi (1 - \sqrt{\phi})^2}} d \tag{37}$$

with d being the diameter of carbon fiber. Thus, if Eq. (31) is used to determine Df, the permeability of GDL is a function depending only on the tortuosity and porosity, which is deduced from the fractal model. The predicted through-plane permeabilities given by Eq. (36) with the tortuosity given by Eq. (29) with $a = 0.714$ and $m = 0.543$ for through-plane is plotted in Fig. 9(b). As shown from this figure, the through-plane permeability predicted from the fractal model is very close to KC relation. However, the fractal model described above cannot accurately predict the in-plane permeability of carbon paper GDL. This may be attributed to the non-representative fractal characteristics of the cross section perpendicular to the in-plane flow direction.

5. Concluding remarks

In this work, the single-phase flow through the carbon paper GDL with anisotropic permeabilities is simulated using the MRT/LBM model. The GDL samples are reconstructed using the stochastic method by considering different porosities and microstructures to imitate different GDL compression ratios and PTFE contents. In-plane and through-plane permeabilities as well as the tortuosity are calculated from the flow field by simulation. The simulated permeabilities match well with the existing measurements in literature. The calculated permeabilities are also compared with empirical relationships, which predict the permeability as a function of porosity and some fitting parameters are determined. In addition, the tortuosity of the carbon paper GDL obtained from simulation also shows the anisotropic characteristic with through-plane tortuosity higher than in-plane. The tortuosity is used in a fractal model to predict the through-plane permeability, and the results indicate that the through-plane permeability of carbon paper GDL based on the fractal model and the KC relation are in good agreement with each other. Compared with the SRT/LBM approach, the results of this paper show that the MRT/LBM approach has the advantages of numerically more stable and viscosity independent when solid boundary is present. Therefore, the MRT/LBM approach is more suitable for simulating flow in porous media at the pore level. Furthermore, because of its kinetic nature, the LBM method is a particularly suitable method to study multiphase and multicomponent flow problems in porous media, which are currently encountered in fuel cell researches. Actually, a few complete LBM simulations [40,41] for single-phase multicomponent flow in solid oxide fuel cells had already been performed. To our knowledge, however, due to the difficulties of simulating multicomponent transport coupling with two-phase transport in PEMFCs, such simulations of PEMFCs are not presented in the literature and further efforts are required in future.

Acknowledgement

References

[1] C.Y. Wang, in: W. Lietsich, A. Lamm, H.A. Gasteiger (Eds.), Handbook of Fuel Cells: Fundamentals, Technology and Applications, vol. 3, part 3, John Wiley & Sons, Chichester, 2003.
[2] P.M. Wilde, M. Mandle, M. Murata, N. Berg, Fuel Cell 3 (2004) 180–184.
[3] W. Lee, C.H. Ho, J.W. Van Zee, M. Murthy, J. Power Sources 84 (1999) 45–51.
[4] D. Bevers, R. Rogers, M.V. Bradke, J. Power Sources 63 (1996) 193–201.
[5] G.G. Park, Y.J. Sohn, T.H. Yang, Y.G. Yoon, W.Y. Lee, C.S. Kim, J. Power Sources 131 (2004) 182–187.
[6] G. Lin, T. Van Nguyen, J. Electrochem. Soc. 152 (2005) A1942–A1948.
[7] M.F. Mathias, J. Roth, J. Feleming, W. Lehnert, in: W. Lietsich, A. Lamm, H.A. Gasteiger (Eds.), Handbook of Fuel Cells: Fundamentals, Technology and Applications, vol. 3, part 1, John Wiley & Sons, Chichester, 2003.
[8] J. Ihonen, M. Mikkola, G. Lindbergh, J. Power Sources 151 (2004) 1152–1161.
[9] M.V. Williams, E. Begg, L. Bonville, H.R. Kunz, J.M. Fenton, J. Electrochem. Soc. 151 (2004) 1173–1180.
[10] J. Pharaoh, J. Power Sources 144 (2005) 77–82.
[11] G. Inoue, Y. Matsukuma, M. Minemoto, J. Power Sources 157 (2006) 136–152.
[12] J.P. Feser, A.K. Prasad, S.G. Advani, J. Power Sources 161 (2006) 404–412.
[13] J.P. Feser, A.K. Prasad, S.G. Advani, J. Power Sources 162 (2006) 1226–1231.
[14] J.T. Gostick, M.W. Fowler, M.D. Pritzker, M.A. Ioannidis, L.M. Behra, J. Power Sources 162 (2006) 228–238.
[15] H.T. Liu, T.H. Zhou, P. Cheng, J. Heat Transfer 127 (2005) 1363–1379.
[16] L.P. Wang, B. Afsharpoya, Math. Comput. Simul. 72 (2006) 242–248.
[17] A.S. Joshi, K.N. Grew, A.A. Peracchio, W.S. Chiu, J. Power Sources 164 (2007) 631–638.
[18] J. Park, M. Matsubara, X. Li, J. Power Sources 173 (2007) 404–414.
[19] C. Pan, L.S. Luo, C.T. Miller, Comput. Fluids 35 (2006) 898–909.
[20] D. d'Humieres, I. Ginzburg, M. Krafczyk, P. Lallemand, L.S. Luo, Philos. Trans. R. Soc. Lond. A 360 (2002) 437–451.
[21] I. Ginzburg, D. d'Humieres, Phys. Rev. E 68 (2003) 066614.
[22] V.P. Schulz, J. Becker, A. Wiegmann, P.P. Mukherjee, C.Y. Wang, J. Electrochem. Soc. 154 (2007) B419–B426.
[23] K. Schladitz, S. Peters, D. Reinel-Bitzer, A. Wiegmann, J. Ohser, Comput. Mater. Sci. 38 (2006) 56–66.
[24] B. Yu, P. Cheng, Int. J. Heat Mass Transfer 45 (2002) 2983–2993.
[25] Y. Shi, J. Xiao, M. Pan, R.Z. Yuan, J. Power Sources 160 (2006) 277–283.
[26] Z. Guo, C. Zheng, B. Shi, Phys. Rev. E 65 (2002) 046308.
[27] Q. Zhou, H.Y. He, Phys. Fluids 9 (1997) 1591–1598.
[28] S. van der Graaf, T. Nisisako, C.G. Schroen, R.G. van der Sman, R.M. Boom, Langmuir 22 (2006) 4144–4152.
[29] A.A. Zick, G.M. Homsy, J. Fluid Mech. 115 (1982) 13–26.
[30] J.T. Gostick, M.W. Fowler, M.A. Ioannidis, M.D. Pritzker, Y.M. Volfkovich, J. Power Sources 156 (2006) 375–387.
[31] B.T. Astrom, R.B. Pipes, S.G. Advani, J. Compos. Mater. 26 (1992) 1351–1373.
[32] M.M. Tomadakis, T.J. Robertson, J. Compos. Mater. 39 (2005) 163–188.
[33] D.L. Johnson, J. Koplik, L.M. Schwartz, Phys. Rev. Lett. 57 (1986) 2564–2567.
[34] P.M. Adler, J.F. Thovert, Appl. Mech. Rev. 51 (1998) 537–585.
[35] A. Koponen, M. Kataja, J. Timonen, Phys. Rev. E 56 (1997) 3319–3325.
[36] A. Koponen, M. Kataja, J. Timonen, Phys. Rev. E 54 (1996) 406–410.
[37] G.L. He, Z.C. Zhao, P.W. Ming, et al., J. Power Sources 163 (2007) 846–852.
[38] B.M. Yu, J.H. Li, Chin. Phys. Lett. 21 (2004) 1569–1571.
[39] P. Xu, B.M. Yu, Adv. Water Resour. 31 (2008) 74–81.
[40] A.S. Joshi, K.N. Grew, A.A. Peracchio, W.K.S. Chiu, J. Power Sources 164 (2007) 631–638.
[41] Y. Suzue, N. Shikazono, N. Kasagi, J. Power Sources 184 (2008) 52–59.